Article

Photocatalytic and Oxidative Synthetic Pathways for Highly Efficient PANI-TiO₂ Nanocomposites as Organic and Inorganic Pollutant Sorbents

Carolina Cionti [1,2], **Cristina Della Pina** [1,3], **Daniela Meroni** [1,2,*], **Ermelinda Falletta** [1,3,*] **and Silvia Ardizzone** [1,2]

[1] Department of Chemistry, Università degli Studi di Milano, via Golgi 19, 20133 Milano, Italy; carolina.cionti@unimi.it (C.C.); cristina.dellapina@unimi.it (C.D.P.); silvia.ardizzone@unimi.it (S.A.)

[2] Consorzio Interuniversitario Nazionale per la Scienza e Tecnologia dei Materiali (INSTM), via Giusti 9, 50121 Florence, Italy

[3] ISTM-CNR, via Golgi 19, 20133 Milano, Italy

* Correspondence: daniela.meroni@unimi.it (D.M.); ermelinda.falletta@unimi.it (E.F.)

Abstract: Polyaniline (PANI)-materials have recently been proposed for environmental remediation applications thanks to PANI stability and sorption properties. As an alternative to conventional PANI oxidative syntheses, which involve toxic carcinogenic compounds, an eco-friendly procedure was here adopted starting from benign reactants (aniline-dimer and H_2O_2) and initiated by ultraviolet (UV)-irradiated TiO_2. To unlock the full potential of this procedure, we investigated the roles of TiO_2 and H_2O_2 in the nanocomposites synthesis, with the aim of tailoring the properties of the final material to the desired application. The nanocomposites prepared by varying the TiO_2:H_2O_2:aniline-dimer molar ratios were characterized for their thermal, optical, morphological, structural and surface properties. The reaction mechanism was investigated via mass analyses and X-ray photoelectron spectroscopy. The nanocomposites were tested on both methyl orange and hexavalent chromium removal. A fast dye-sorption was achieved also in the presence of interferents and the recovery of the dye was obtained upon eco-friendly conditions. An efficient Cr(VI) abatement was obtained also after consecutive tests and without any regeneration treatment. The fine understanding of the reaction mechanism allowed us to interpret the pollutant-removal performances of the different materials, leading to tailored nanocomposites in terms of maximum sorption and reduction capability upon consecutive tests even in simulated drinking water.

Keywords: Nanocomposites; Hybrid nanoparticles; polyaniline; titanium dioxide; pollutant sorption; green synthesis.

1. Introduction

Polyaniline (PANI) is one of the most appealing members of the intrinsically conductive polymer family thanks to its unique features, such as high stability, acid-base characteristics and peculiar redox properties. For all these reasons, PANI-based materials and composites are now a hot-topic in the materials science community and have been applied in numerous fields, ranging from photovoltaics, anticorrosion and biomedical devices to sensors, electrochemistry and electronics [1–11]. Furthermore, in recent years PANI has drawn increasing attention as alternative sorbent for pollutant remediation from both water and air due to its high sorption capability and ease of regeneration [12–16]. In this regard, polyaniline represents a promising alternative to

currently adopted materials, such as activated carbon, thanks to the fact that PANI does not require energy-consuming thermal activation and regeneration treatments.

On the other hand, PANI traditional synthesis involves noxious and toxic reagents (aniline monomer and strong oxidants such as $(NH_4)_2S_2O_8$), leading to carcinogenic by-products (benzidine and trans-azobenzene) and producing large amounts of inorganic waste during the product purification (mostly sulphates). Some attempts were carried out to find alternative green procedures. Among them, the enzymatic route based on the metal-enzyme Laccase is attractive but still remains a method for small-scale preparation [17]. More interestingly, the electrochemical preparation of PANI has been extensively explored. This latter method represents the best approach to produce PANI films characterized by a fine control of thickness and morphology [18]. However, electrochemical syntheses show lower production yield than chemical oxidation, do not permit the production of complex polymer-inorganic composites, and present difficulties in scale-up [18,19]. In order to achieve high production yields, long-term electropolymerization is needed: this procedure leads to the accumulation of by-products including p-benzoquinone, p-hydroquinone and co-oligomers of aniline and p-benzoquinone and acid [18]. Besides their significant side effects on the properties of the final product, the discarded electrolyte solution is highly pollutant. As an alternative, an environmentally friendly process was developed by some of us [14] adopting more benign compounds, such as aniline dimer (N-(4-aminophenyl)aniline) as starting reagent, H_2O_2 as oxidant and $FeCl_3$ as catalyst. Even though aniline dimer is produced by chemical routes and labeled as toxic and irritant, it is not carcinogenic, differently from aniline monomer, and its solid form makes handling easier and safer. Furthermore, PANI synthesis by aniline dimer leads to H_2O as the only co-product thus simplifying the material post-treatment and eliminating the production of carcinogenic species. However, because of the fast polymerization, this procedure does not allow a strict control over the polymer structural and morphological features and the resulting polyaniline is characterized by a compact morphology, low surface area and, as a consequence, poor sorption properties. Very recently, we developed a new green, two-step synthesis taking advantage of the photocatalytic properties of TiO_2 semiconductor under UV irradiation [20]. The outstanding properties of the resulting PANI-TiO_2 nanocomposite, including unique PANI crystallinity, high surface area and porosity, prompted us to further investigate these promising composite materials.

Here, PANI-TiO_2 nanocomposites were prepared by varying the stoichiometric amounts of the two main actors of this procedure, TiO_2 and H_2O_2, with the aim of tailoring the physicochemical properties of the final material. Differences among the various products were highlighted by an all-round characterization including structural, morphological, thermal, and optical analyses. Moreover, we took advantage of the unique opportunity offered by the present synthetic approach, in which the oligomerization and polymerization steps are clearly separated, to investigate the early stages of PANI synthesis. Samples were characterized after the oligomerization step by a combination of spectroscopic and spectrometric techniques to disentangle the photocatalytic and catalytic TiO_2 contributions. Finally, we demonstrate the nanocomposites ability to remove both organic (methyl orange) and inorganic (Cr(VI)) pollutants in water and in a wide concentration range; the materials reusability was also evaluated without any regeneration treatment, also in conditions closer to real life usage. The fine understanding of the reaction mechanism allowed us to interpret the pollutant removal performance of the different materials, leading to tailored nanocomposites in terms of maximum sorption capability upon consecutive tests even in simulated drinking water.

2. Materials and Methods

Sigma Aldrich (Darmstadt, Germany) reagents were adopted for experimental procedures, unless specified otherwise. Suspensions and solutions were prepared with Milli-Q water.

2.1. Sample Preparation

PANI-TiO_2 nanocomposites were synthesized by a two-step green method. In a typical synthesis, 1 g of aniline dimer (*N*-(4-aminophenyl)aniline) was dissolved in 290 mL of a 0.09 M HCl

aqueous solution. Then, 175 mg of P25 TiO_2 (Evonik, Bitterfeld, Germany) was added under vigorous stirring and irradiated with UV light (halogen lamp 500 W Jelosil, Vimodrone, Italy; 30 mW cm^{-2}) for 135 min. Then, the suspension was stirred in the dark for 4 h at 25 °C. In the second step, 0.55 mL of 30% H_2O_2 aqueous solution was added and the reaction mixture was stirred for 18 h in the dark. The final product was collected by filtration and washed with 50 mL of water and few milliliters of acetone, then dried at room temperature overnight. Hence, this sample, named 1 × 1 in the following, was prepared using TiO_2:H_2O_2:aniline dimer molar ratios = 0.4:1.0:1.0.

In order to disentangle the relative contributions of TiO_2 and H_2O_2, different samples were prepared by modulating the TiO_2:H_2O_2:dimer molar ratios while keeping all other parameters unchanged (aniline dimer concentration, HCl amount, temperature, irradiation time). Samples were labelled as *n* × *m* where *n* is a number indicating the TiO_2 molar amount with respect to the reference synthesis (i.e., ratio between the adopted TiO_2 moles and the TiO_2 moles in the 1 × 1 reference), while *m* indicates the H_2O_2 amount also compared to the reference sample (i.e., adopted moles of H_2O_2 divided by the H_2O_2 moles used in 1 × 1 reference). In a first series, the amounts of both TiO_2 and H_2O_2 were doubled (2 × 2) and tripled (3 × 3). Another set of samples was prepared by varying only the photocatalyst quantity, doubling (2 × 1) and tripling it (3 × 1). The last series was obtained by doubling and tripling only the H_2O_2 amount (1 × 2 and 1 × 3, respectively). For better clarity, Table 1 lists the prepared nanocomposites, along with the reactant molar ratios.

For the sake of comparison, PANI-TiO_2 composites were compared with a pure PANI sample (named PANI_ref) prepared according to the green synthetic approach previously proposed by some of us, using aniline dimer, H_2O_2 (H_2O_2 : dimer molar ratio = 5) and $FeCl_3$ catalyst [14].

Table 1. Stoichiometric molar ratios of photocatalyst and H_2O_2 with respect to aniline dimer (columns 2 and 3), weight percentage of PANI and TiO_2 in the final products obtained from TG analyses (columns 4 and 5), measured specific surface area of each composite and calculated surface area of a physical mixture with same composition (columns 6 and 7).

| Sample | Molar ratios | | Sample composition[1] | | S_{BET} | S_{BET} mix [2] |
	TiO_2/dimer	H_2O_2/dimer	%PANI	%TiO_2	$(m^2 g^{-1})$	$(m^2 g^{-1})$
1 × 1	0.4	1.0	58	31	44.8	17.2
2 × 2	0.8	2.0	52	38	32.8	20.6
3 × 3	1.2	3.0	43	50	24.0	26.3
2 × 1	0.8	1.0	34	61	40.5	31.5
3 × 1	1.2	1.0	27	69	41.0	35.3
1 × 2	0.4	2.0	64	24	20.8	13.9
1 × 3	0.4	3.0	75	15	6.0	9.8

[1] The sum of %PANI and %TiO_2 is lower than 100 because of water and dopant content.
[2] Surface area of theoretical mechanical mixtures with the same composition of the samples, calculated as the weighted sum of PANI_ref and TiO_2 surface area, taking into account the sample composition determined from TGA.

2.2. Materials Characterization

X-ray powder diffraction (XRPD) analyses were carried out with a PW 3710 Bragg-Brentano goniometer (Philips, Amsterdam, The Netherlands) equipped with a scintillation counter, a slit with 1° divergence, a receiving slit of 0.2 mm and a 0.04° Soller slit system. A graphite-monochromatic Cu Kα radiation was adopted at a nominal X-ray power of 40 kV × 40 mA. Diffractograms were obtained in a 2θ range between 10° and 80°.

A UV-2600 UV-vis spectrophotometer (Shimadzu, Kyoto, Japan) was employed to record UV-vis absorption spectra in the 200–1000 nm range of samples dissolved in DMF with and without HCl addition.

Fourier Transform infrared (FTIR) spectra were collected in the 400–4000 cm^{-1} range using a Spectrum 100 ATR spectrometer (PerkinElmer, Waltham, MA, USA).

The Brunauer-Emmett-Teller (BET) method was adopted to determine the composite specific surface area from adsorption isotherms of N_2 in subcritical conditions, measured using a SA3100 instrument (Beckman-Coulter, Brea, CA, USA).

A LEO 1430 instrument (Zeiss, Jena, Germany) was employed to acquire Scanning Electron Microscopy (SEM) images.

Thermo gravimetric analyses (TGA) were performed in air (5 °C min^{-1}, temperature range 30–900 °C) with a TGA/DSC 3+ instrument (Mettler Toledo, Switzerland) equipped with a 70 μL alumina crucible.

An M-probe apparatus (Surface Science Instruments, Pasadena, CA, USA) was adopted for X-ray photoelectron spectroscopy (XPS) analyses: the source was a monochromatic Al Kα radiation (1486.6 eV). The accuracy of the reported binding energies (B.E.) can be estimated as ± 0.2 eV. Peak fitting was carried out using combined Gaussian−Lorentzian curves, upon background correction with the Shirley method. Binding energies were corrected for specimen charging by referencing the Ti(IV) component of the Ti $2p_{3/2}$ peak at 458.5 eV.

Electrospray ionization spectrometry (ESI-MS) analyses were conducted on an ion trap mass spectrometer (LCQ Fleet, Thermo Scientific, Waltham, MA, USA) operating in the positive ion mode. Aliquots were directly infused into the ESI source at a flow rate of 20 μL min^{-1} by a micro syringe. The ESI source conditions were as follows: heated capillary temperature 295 °C; sheath gas (N_2) flow rate 4 L min^{-1}; spray voltage 5.5 kV; tube lens offset voltage 95 V. The m/z range employed in all experiments was 50–2000.

2.3. Study Of The Reaction First Step

In order to investigate the first stage of the reaction, two tests were performed by stopping the reaction before the addition of H_2O_2, in order to characterize the formed oligomers via FTIR and XPS analyses. In one test, by following the reference (1 × 1) synthetic procedure, TiO_2 powder was suspended in an aqueous solution of the aniline dimer, acidified by HCl, and was irradiated with UV light for 2.25 hours. After irradiation, the reaction was stopped by centrifugation and the solid fraction was retrieved and characterized. The second test was carried out in the same way, but without UV irradiation: the suspension was kept in the dark under stirring for 2.25 hours after TiO_2 addition and then centrifuged.

2.4. Dye-Removal Tests

The nanocomposites sorption capabilities were tested towards methyl orange (MO) removal in water medium without any direct irradiation . For each composite, 50 mg of sample was suspended in 20 mL of a MO solution (10–200 ppm) for 20 minutes (at spontaneous pH, around 5, and room temperature) and then recovered by centrifugation. The remaining dye concentration was determined by UV-vis spectroscopy at the wavelength of maximum absorption (504 nm).

The influence of electrolytes was studied by performing sorption tests both in Milli-*Q* water and in simulated drinking water, prepared according to Annex B2 of the Second Protocol of the French Norm NF P41-650 regarding the Specifications for Water Filter Pitchers (Table S1)[21].

Consecutive sorption tests were performed without regenerating the sample between tests: powders were simply retrieved by centrifugation at the end of the sorption step and re-suspended in MO solution for the next dye removal test without accounting for any powder loss.

2.5. Cr(VI) Remediation Tests

The Cr(VI) abatement capability was tested in water with two different Cr(VI) concentrations, 10 and 50 ppm, and without any direct irradiation. 50 mg of sample was suspended in 20 mL of a $K_2Cr_2O_7$ aqueous solution for 20 minutes and then recovered by centrifugation. After that, the sample was resuspended in other 20 mL of Cr(VI) solution for a consecutive chromium-removal test without any regeneration treatment: this cycle was repeated five times. The remaining Cr(VI) concentration was determined by UV-vis spectroscopy at the wavelength of maximum absorption

(540 nm): before the analysis, 10 mL of the solution retrieved by centrifugation was treated with 200 µL of a 0.5% diphenylcarbazide (DFC) solution and 100 µL of a 0.1 M H_2SO_4 solution and let at rest for 15 min.

The total chromium content (hexavalent and trivalent) in solution was evaluated by atomic absorption spectroscopy (AAS). The analyses were carried out on a PinAAcle 900 T spectrometer (Perkin Elmer, Waltham, MA, USA) using air-acetylene flame and working with a wavelength of 357.87 nm.

3. Results

In order to better understand the reaction pathway and tailor the materials properties to the desired application, the role of TiO_2 and H_2O_2 ratios with respect to aniline dimer are herein investigated. With this aim, seven different samples were prepared as reported in Table 1. It should be noted that, when the reaction is carried out in the absence of TiO_2, hardly any material could be produced [20].

3.1. Thermogravimetric Analyses

In agreement with the literature regarding doped PANI thermal degradation, TG analyses performed in air of all composites showed three main weight loss stages [22–25] (Figure 1): the first at around 100 °C is attributed to the loss of physisorbed water, the second one (150–200 °C) is due to the loss of the dopant (HCl), and the third one, which accounts for most of the weight loss, starts at around 350 °C and is attributed to the polymer backbone degradation. At 700 °C, PANI is fully degraded in all samples, therefore the remaining fraction can be attributed to TiO_2 [26]; in this way, we could evaluate the actual composition of the samples (Table 1, columns 4 and 5).
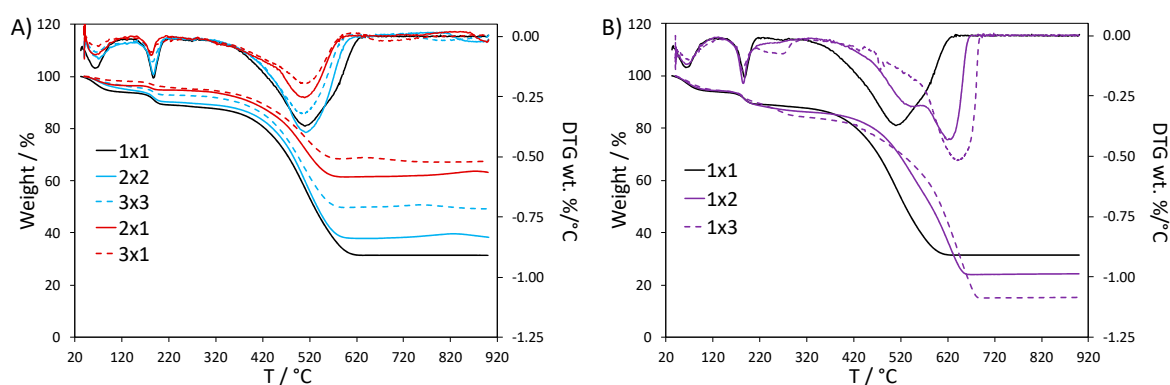

Figure 1. TGA and DTG curves of PANI-TiO_2 nanocomposites: (**A**) effect of TiO_2 quantity and (**B**) effect of H_2O_2 amount.

By comparing the samples prepared with the same stochiometric amount of TiO_2, such as 1 × 1, 1 × 2 and 1 × 3, we could expect the same %TiO_2 in these composites, but this is not the case: increasing the amount of H_2O_2 leads to a higher PANI content. This trend can be also observed by comparing 2 × 1with 2 × 2 sample (34%w and 52%w of PANI, respectively) and 3 × 1 with 3 × 3 sample (27%w vs. 43%w of PANI). These results support a promoting role of H_2O_2 on PANI formation.

Differences in the thermal stability of the composites can be better appreciated by comparing the weight loss derivative (DTG) curves (Figure 1). The composites with higher TiO_2 content showed the same DTG profile as the reference 1 × 1 sample (Figure 1A), where water desorption, HCl loss and polymer degradation give rise to peaks at 70, 187 and 510 °C, respectively [22,27–29]. Similar results are observed when both the TiO_2 and H_2O_2 amounts are increased. On the other hand, when only the H_2O_2 amount is increased, a second peak component with higher thermal stability is appreciable for the polymer chain degradation (1 × 2 and 1 × 3 in Figure 1B): this second component becomes more important and progressively shifted to higher temperature by increasing the H_2O_2

quantity (625 and 640 °C for 1 × 2 and 1 × 3, respectively). Moreover, the DTG curve of the 1 × 3 sample presents also a peak at 267 °C, which could be attributed to HCl bound in a stronger way to the polymer backbone or to oligomer chains degradation. It is noteworthy that the DTG curve of PANI_ref (Figure S1) displays broader peaks with respect to the 1 × 1 curve, both in the case of dopant loss and of the polyaniline chain degradation. In particular, DTG peak components at higher temperatures are appreciable, similarly to the case of the 1 × 2 and 1 × 3 curves.

The thermal stability of PANI is known to be affected by several factors, such as the structure of the polymer backbone and oxidation state [22,30–32]. In the literature, the presence of interactions between PANI chains and TiO_2 surface is reported to weaken the polyaniline inter-chain interactions, thus lowering the thermal stability of the composite [23,24,27,30,31,33,34]. This can explain the lower thermal stability of our composites with respect to PANI_ref. However, when the TiO_2 : H_2O_2 ratio is weighted in favor of H_2O_2 (as in 1 × 2 and 1 × 3 samples), the thermal stability becomes comparable with PANI_ref, supporting the occurrence of weakened polymer-TiO_2 interactions, possibly due to different composite formation mechanisms (vide infra).

3.2. Structural Properties

The structural properties of all the composites were investigated via XRPD analyses (Figure 2): all the diffractograms showed the peaks of both TiO_2 (anatase and rutile phases) and polyaniline.

The reference composite (1 × 1) presented sharp and well resolved peaks of the ES-I form of the emeraldine salt [35], characteristic of a high crystallinity degree. The presence of well defined peaks due to crystalline PANI phases, which are far less resolved in both PANI_ref [14] and in PANI from oxidative aniline polymerization [35], is indicative of a more ordered arrangement of the polymer chains in the composite samples with respect to pure PANI. It should be noted that our composites are far more crystalline than PANI composites prepared via traditional oxidative polymerization in the presence of TiO_2 or even other oxides [28,36–40]. This observation supports the occurrence, in the present case, of a different reaction mechanism promoted by the photocatalytic properties of the oxide semiconductor under UV irradiation.

By increasing both the amounts of photocatalyst and H_2O_2 (Figure 2A), the polymer XRPD peaks decrease in relative intensity with respect to TiO_2 reflections: this can be only partly explained by the lower PANI content (Table 1). Moreover, particularly in the 3 × 3 composite, PANI peaks loose resolution, suggesting a lower crystallinity degree of the polymer.

Samples 2 × 1 and 3 × 1 (i.e., with increased amount of only TiO_2) showed similar diffractograms, with PANI peaks less intense than 1 × 1 (in agreement with their lower PANI content, Table 1), but still clearly resolved (Figure 2B).

Conversely, the composites with increased amount of only H_2O_2 (1 × 2 and 1 × 3) displayed less defined and overlapped PANI peaks with respect to the 1 × 1 sample (Figure 2C). In particular, in the sample 1 × 3, the fine structure of the polyaniline peaks is nearly lost, indicating a more amorphous arrangement of the polymer chains as also supported by the clearly appreciable amorphous halo.
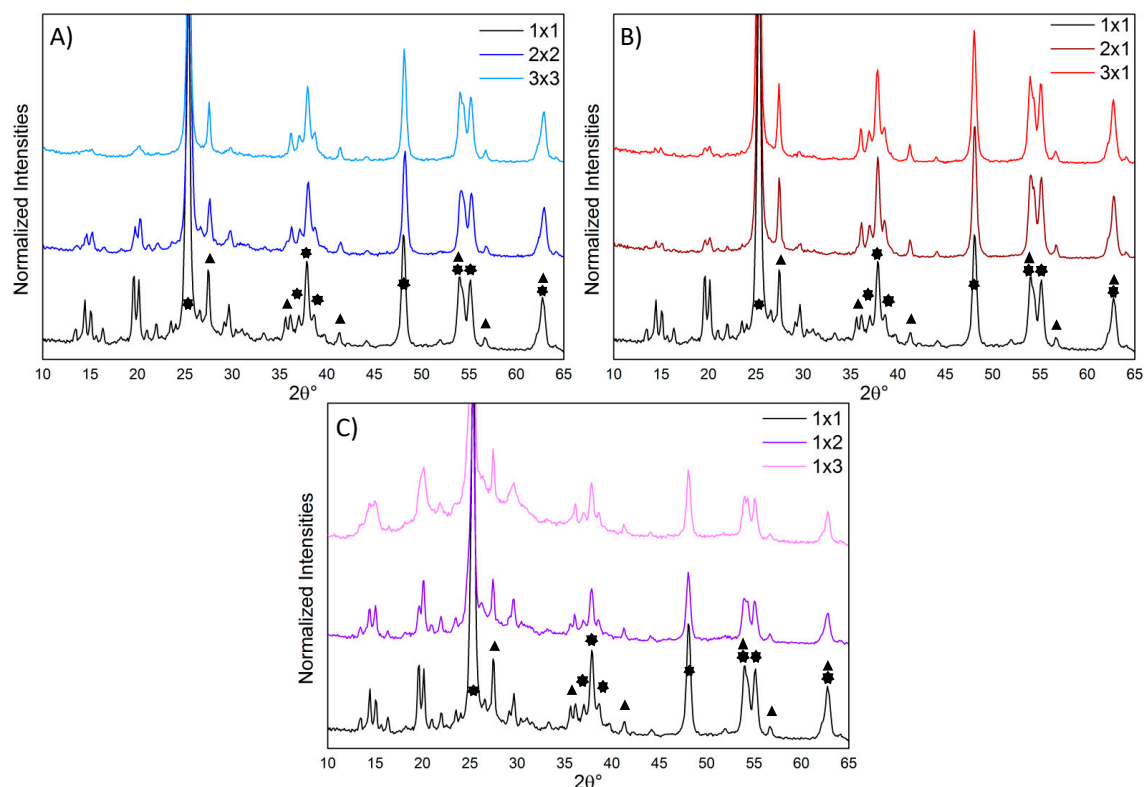
Figure 2. Normalized XRPD diffractograms (with respect to the anatase TiO_2 (213) peak): **A**) effect of changing both the TiO_2 and H_2O_2 amounts; **B**) effect of changing only the TiO_2 amount; **C**) effect of changing only the H_2O_2 amount. The stars and triangles highlight the peaks related to the TiO_2 crystalline phases (anatase and rutile, respectively [41]).

In accordance with TGA results, increasing the amount of TiO_2 does not significantly affect the composite properties, whereas when the TiO_2 : H_2O_2 ratio is decreased, a notable effect on the PANI crystallinity is observed.

3.3. Morphological Properties

N_2 adsorption isotherms under subcritical conditions (T = -196 °C) were acquired to evaluate the specific surface area of all samples by the BET method (Table 1). It is noteworthy that all samples show a much larger surface area with respect to PANI_ref (3 $m^2 g^{-1}$). In this respect, the acquired surface area of each composite was compared to the surface area of a hypothetical mechanical mixture with the same composition, calculated as the weighted sum of S_{BET} values of TiO_2 (50 $m^2 g^{-1}$) and of PANI_ref [42]. All calculated values are lower than the experimental ones, with the only exceptions of 3 × 3 and 1 × 3 composites. On these grounds, we can assert that the composites are not simple mechanical mixtures, but the observed synergistic effect on morphology supports an active role of TiO_2 in the polymer formation. It is worth noting that the two exceptions are represented by the samples with the highest H_2O_2/aniline dimer molar ratios.

The variation of the composite surface area with the H_2O_2/aniline dimer molar ratio is reported in Figure 3. As observed in the case of XRPD analyses, the variation in the photocatalyst amount does not significantly affect the properties of the composites: in fact, samples 1 × 1, 2 × 1 and 3 × 1 have comparable surface areas (blue stars in Figure 3). On the contrary, when the H_2O_2 quantity is increased, the specific surface area shows a clear decreasing trend. While the surface area lowering is less marked for the 2 × 2 and 3 × 3 composites (red triangles in Figure 3), the BET area drastically drops to few square meters (similarly to PANI_ref, 3 $m^2 g^{-1}$) when only the H_2O_2 amount is increased (green dots in Figure 3).
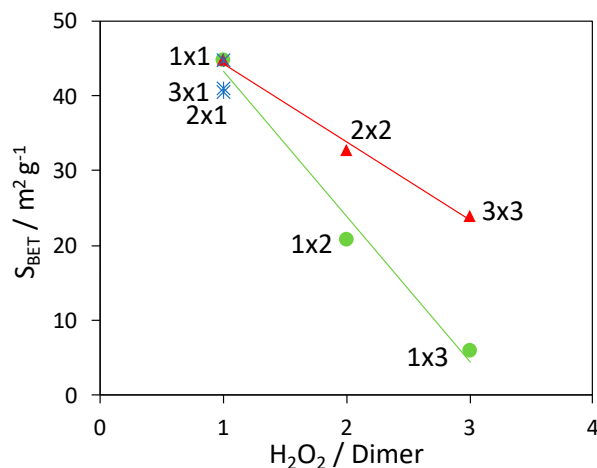
Figure 3. Dependence of the composite surface area vs. the H_2O_2/aniline dimer molar ratio: effect of changing the H_2O_2 amount (green dots), TiO_2 content (blue stars), and of varying both parameters (red triangles). Lines are added as a guide for the eye.

Therefore, as it was for crystallinity and thermal stability, the surface area is influenced mainly by the H_2O_2 amount while its effect can be partially compensated by the simultaneous increase of TiO_2 amount.

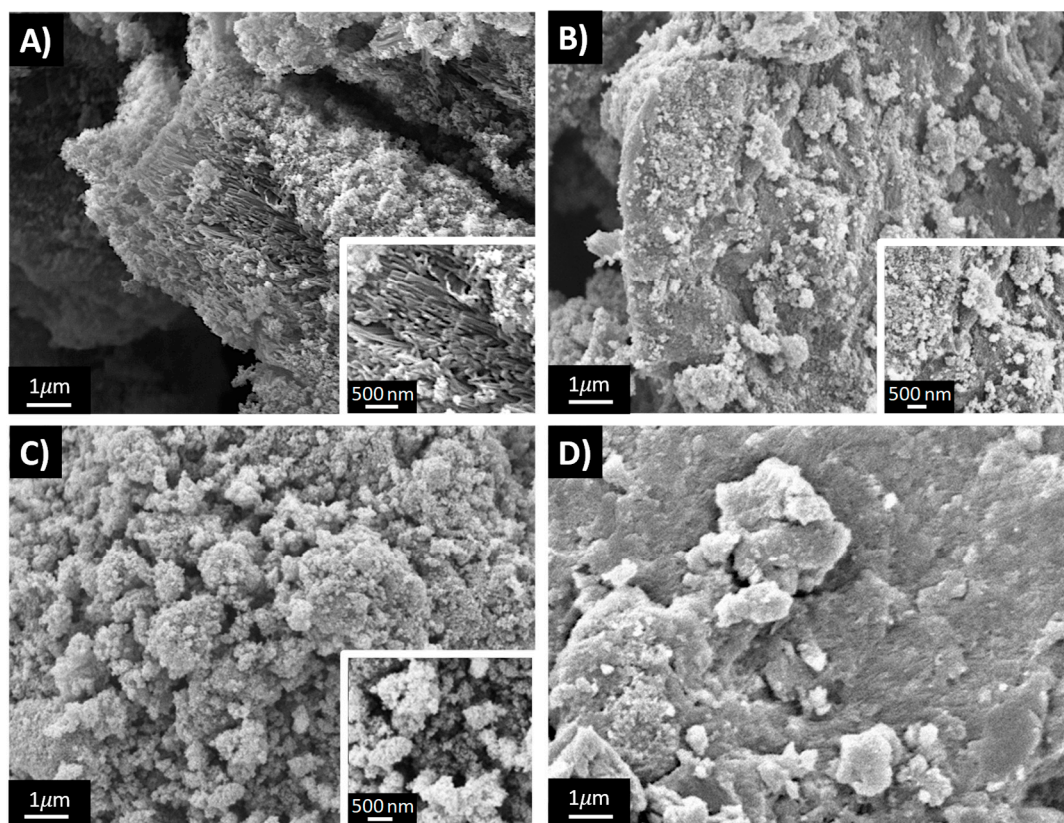Figure 4 reports the SEM images of four PANI-TiO$_2$ composites: 1 × 1, 3 × 3, 3 × 1 and 1 × 3.

Figure 4. SEM images of: **A**) 1 × 1, **B**) 3 × 3, **C**) 3 × 1, **D**) 1 × 3.

In agreement with BET results, the morphology of the materials is mainly influenced by the H_2O_2 amount used for their synthesis. In fact, 1 × 1 (Figure 4A) and 3 × 1 (Figure 4C) samples exhibit a similar sponge-like nanostructured morphology characterized by nanorod morphological structures, as clearly shown in Figure 3A inset. On the contrary, the 1 × 3 sample (Figure 4D) is characterized by larger and smooth aggregates, whereas the 3 × 3 sample displays intermediate

morphological characteristics (Figure 4B). It should be noted that the reference sample (PANI_ref) presents an even more compact morphology characterized by micrometric and smooth particles [14].

3.4. FTIR Spectroscopy

FTIR spectra (Figure S2) confirm the successful formation of PANI in all composite samples. The ratio between C=C bands of quinoid and benzenoid rings of PANI (at 1570 and 1489 cm^{-1}, respectively) is consistent with the presence of PANI mainly in the emeraldine form, in agreement with XRPD results. Other characteristic bands are the C-N bending vibration in aromatic amines at about 1300 cm^{-1}, the in-plane and out-of-plane bending modes of C-N at 1030 and 875 cm^{-1}, and the stretching mode of N=Q=N (Q = quinoid ring) at around 1000 cm^{-1} [43]. Moreover, the broad band in the 3400-1800 cm^{-1} region is indicative of highly conjugated structures [44]. It is noteworthy that no signals are appreciable in the 3600-3700 cm^{-1} region characteristics of oxide surface hydroxyl groups [45]. In this respect, Figure S3 compares the FTIR spectrum of the composite with the highest TiO_2 content (3 × 1, about 70%w) with those of PANI_ref and pristine TiO_2, better highlighting the absence of the oxide surface hydroxylation in the composite. Conversely, when a conventional oxidative polymerization is adopted for the synthesis of PANI-TiO_2 composites [12], the oxide surface hydroxylation is clearly visible in FTIR spectra. The absence of the oxide surface hydroxylation band in our composites suggests a complete coverage of the TiO_2 particles by polyaniline chains, supporting a strong interaction between the oxide surface and the polymer (see XPS results in Section 3.7).

The band at 1240 cm^{-1} is related to the C-N$^+$ stretching vibration in the polaron structure of conducting PANI [44]. A high degree of electron delocalization is also testified by the strong band at around 1140 cm^{-1}, described as "electron-like band" of PANI [46], that can be observed for all composites.

At wavenumbers lower than 900 cm^{-1}, the broad band of TiO_2 (Figure S3) is predominant in composite samples, making difficult to appreciate overlapping bands characteristic of PANI, such as the deformation vibration modes for the aromatic rings at 741 and 689 cm^{-1} or that at 573 cm^{-1}, typical of 1,4 di-substituted benzene. The TiO_2 band in the 900–400 cm^{-1} region becomes more intense for samples with higher TiO_2 content, in good agreement with TGA results.

3.5. UV-vis Spectroscopy

UV-vis spectra of samples are reported in Figure S4. According to the literature [14,47], spectra acquired in both DMF solution (Figure S4A) and acidified DMF (Figure S4B) show the typical bands of polyaniline in its emeraldine form, as confirmed by the band at 430 nm, assigned to polaron–π^* transitions.

More in detail, in Figure S4A the band at 320 nm can be assigned to the $\pi \rightarrow \pi^*$ transition of benzenoid rings (H1), whereas that at 585 nm is due to the benzenoid to quinoid excitonic transition (H2), shifted at 890 nm when the spectra are collected in acidic conditions (Figure S4B). The intensity ratio of the two bands represents an index of the oxidation state of the polymer. For PANI_ref, the H1/H2 ratio was determined to be 2.65 (Figure S4C). Figure 5 and Table S2 show the dependence of the H1/H2 ratio from the H_2O_2/aniline dimer molar ratio.
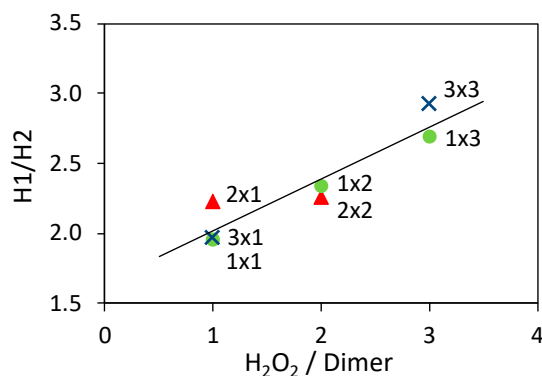
Figure 5. Dependence of the H1/H2 ratio from the H_2O_2/aniline dimer molar ratio. Samples prepared using the same TiO_2 amount are represented with the same marker and the line is added as guide for the eyes.

The results indicate that the use of a large amount of H_2O_2 during the composite synthesis increases the benzenoid/quinoid ratio, to the detriment of the ideal 1:1 ratio of the emeraldine form. On the other hand, the amount of photocatalysts plays no significant role in this regard.

3.6. Mass Spectra

Mass spectra of the DMF-soluble fractions of 1 × 1, 1 × 2, 1 × 3 and 3 × 1 samples are reported in Figure 6; the relative MS spectrum of PANI_ref sample is reported for the sake of comparison. Although only the soluble fractions, hence short chains, are responsible for acquired data, such information can be precious to investigate the polymerization pathways.
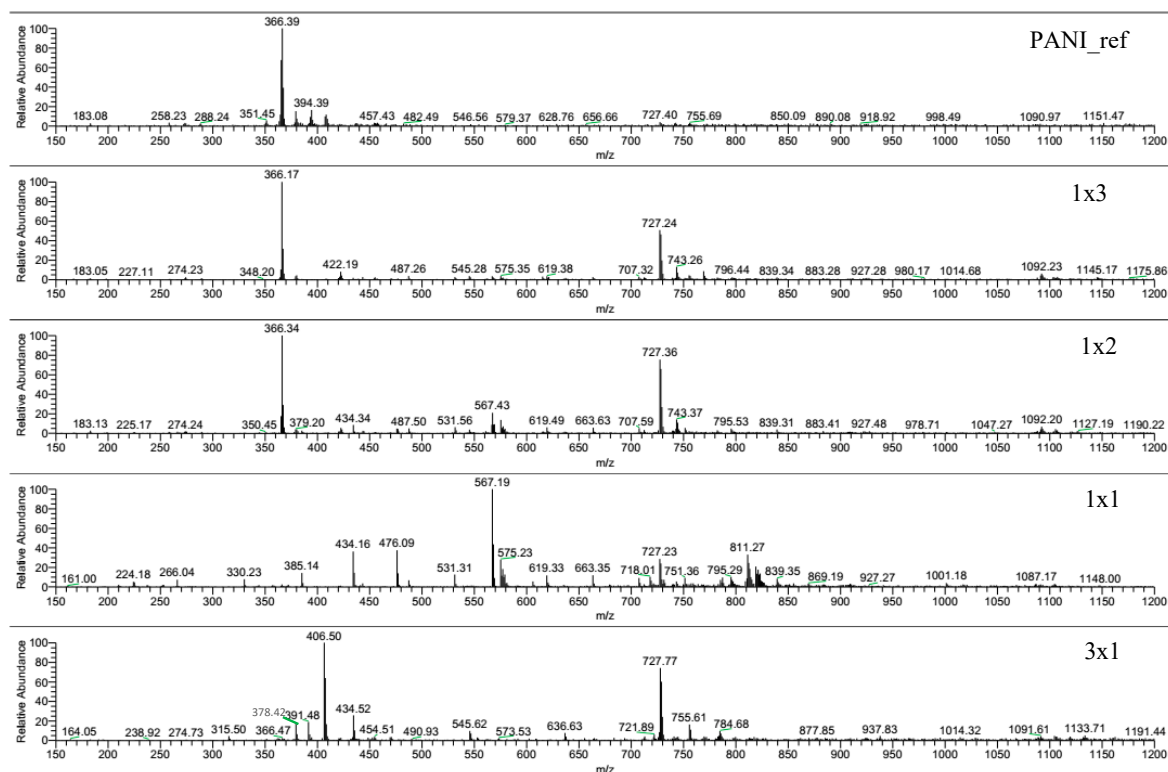

Figure 6. MS spectra of DMF-soluble fractions of PANI_ref, 1 × 3, 1 × 2, 1 × 1, and 3 × 1 samples.

When the reaction is carried out in the presence of a large amount of H_2O_2 (PANI_ref, 1 × 3 and 1 × 2), an intense peak at 366 m/z is observed, which can be attributed to linear tetramers (Table S3) [48]. This is the only peak appreciable in the PANI_ref spectrum, whereas the MS spectra of 1 × 2 and 1 × 3 samples present three other peaks at 727, 743 and 1092 m/z, which can be assigned to linear octamers and linear dodecamers [49]. By increasing the TiO_2/H_2O_2 ratio (1 × 1 and 3 × 1 samples), the

peak of linear tetramers (366 m/z) disappears replaced by other peaks, e.g. at 434 m/z. As for the 1 × 1 spectrum, the 567 m/z peak can be attributed to sodium adducts of oxidized hexamers [49], while peaks at 434 and 811 m/z can be explained by the presence of hydroxylated chains (Table S3), as also supported by XPS (see Section 3.7). Moreover, the MS spectrum of the 3 × 1 sample shows other peaks, such as those at 406 and 378 m/z, which could be explained by structures formed by consecutive C=O removal from aromatic rings, causing ring contraction (Table S3), possibly due to radical induced reactions.

3.7. Study Of The Oligomerization Step

Drawing information about the reaction mechanism from the final polymer is difficult due to its low solubility, the complexity of its long chain interactions and spatial orientation. The present synthetic approach offers an opportunity to investigate the early stages of PANI synthesis, as the polymerization step occurs only upon H_2O_2 addition.

In the oligomerization step, the photocatalytic effect of TiO_2 seems to play a main role as the same synthetic procedure performed without UV irradiation leads to composites with only minor PANI content [20]. Therefore, the first stage of the reaction (before H_2O_2 addition) was investigated via FTIR and XPS analyses on two samples: the first one was prepared by stopping the synthetic procedure after 135 min of UV irradiation (labeled as UV), the second one was obtained in the same way but without UV irradiation (NoUV). The pristine oxide was adopted as reference.

FTIR spectra of UV and NoUV samples (Figure S5) present the same bands at around 1590, 1505, 1325 and 1160 cm^{-1} besides a broad band from 3600 to 2000 cm^{-1}. The latter is indicative of a more extended conjugation with respect to the dimer molecules, whereas in the 1600-1100 cm^{-1} region the peak positions are intermediate between those of the dimer and the polyaniline. Below 800 cm^{-1} the intense and broad signal related to TiO_2 is predominant. The clear differences between UV and NoUV spectra and those of aniline dimer and 1 × 1 composite support, in the former, the growth of oligomeric species on the TiO_2 particle surface, as also shown by the violet color of the suspension before H_2O_2 addition, typical of PANI oligomers.

On the other hand, XPS analyses presented notable differences between the two samples. The sample surface composition, as determined from survey spectra, is reported in Table S4. Both the UV and noUV samples show similar surface composition, with a larger carbon content for the noUV composite.

In the Ti 2p region (Figure 7A), both UV and NoUV samples showed two components: the component at lower B.E., which is the only one present in pristine TiO_2, is attributed to Ti(IV), also on the ground of the spin-orbit splitting value of 5.7 eV; the second component at higher B.E. has been previously reported [50] also in the case of PANI-TiO_2 composites [51]. This shifted component is prevalent in the UV sample (72%), though it has a high relative weight also in the NoUV sample (49%) (Table 2). In the literature, aniline and diazobenzene adsorption on TiO_2 anatase and rutile single crystal surfaces has been reported to lead to a positive shift of titania bands upon direct interaction of the N atom of the organic molecule with the titania surface [52,53]. Although the here reported shift is more pronounced, it can be related to the surface adsorption of aniline dimer and of oligomer species, which thus seems to be favored by UV-irradiation.
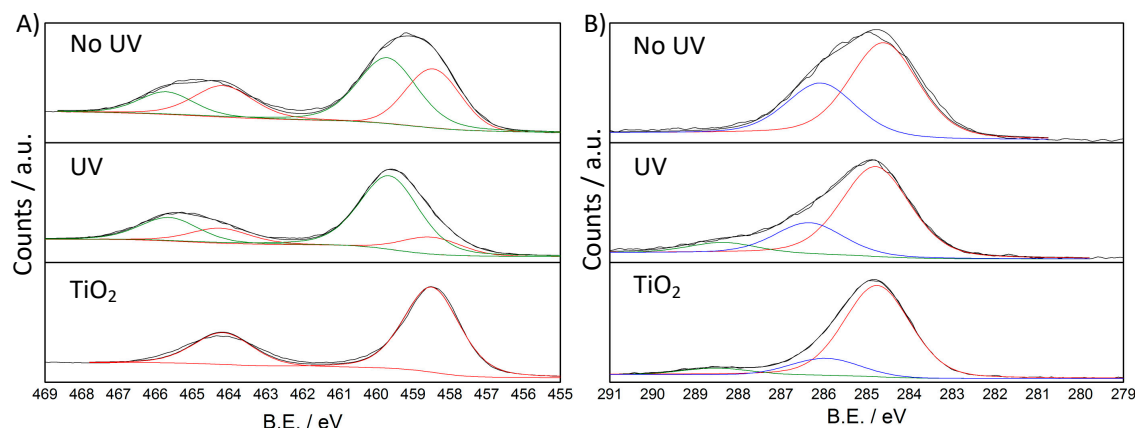
Figure 7. High resolution XPS spectra, and relative fitting, of NoUV, UV and TiO₂ samples: **A**) Ti 2p region and **B**) C 1s region.

Table 2. B.E. and peak area of the components of the UV and NoUV samples compared to pristine TiO₂.

Region	TiO₂		NoUV		UV	
	Position (eV)	% Area	Position (eV)	% Area	Position (eV)	% Area
Ti 2p	458.5	100	458.5	51	458.5	28
	-		459.7	49	459.7	72
C 1s	284.7	81	284.6	65	284.8	68
	285.9	14	286.1	35	286.4	24
	288.4	5	-		288.4	8
O 1s	529.7	85	529.8	57	530.1	53
	531.4	15	531.2	43	531.2	39
	-		-		532.9	8

In the C 1s region, pristine TiO₂ displays the characteristic components due to adventitious carbon [45]. Spectra of both NoUV and UV samples showed a main component at 284.7 ± 0.1 eV which can be attributed to C-C and C-H species [54], and a second major component at ca. 286 eV due to more oxidized carbon, which can be related to the C-N/C=N bonds (Table 2) [55,56]. It is noteworthy that the UV composite shows a third component at higher B.E. (288.4 eV), which could be attributed to highly oxidized carbon bonded with oxygen [45] (Figure 7B). The latter attribution is also supported by O 1s region (Figure S6A) and closely reflects MS findings.

In the O 1s region, all three samples present a main component at around 530 eV attributable to bulk lattice oxygen (Ti-O-Ti) [45,50]. A second more oxidized component at around 531 eV can be appreciated in all three samples and attributed to surface oxygen species: in the pristine TiO₂ sample, this component can be attributed to hydroxyl groups [45,50], also on the ground of FTIR spectra (Figure S5). The lattice oxygen relative abundance is higher in pristine TiO₂ (85%) than in NoUV and UV samples (57% and 53%, respectively): this observation can be referred to signal attenuation in the latter samples, due to the adsorbed organic species at the TiO₂ surface. As in the case of the C 1s region, the UV sample shows a third more oxidized component (532.9 eV), accounting for about 8% of total oxygen species (Table 2), which can be attributed to oxidized carbon species (Figure S6A)[56].

The N 1s region of UV and NoUV samples (Figure S6B) displays a broad and less intense peak: for these reasons we preferred not to fit the N 1s signal to avoid possible misleading interpretations. In any case, a clear shift towards higher B.E. is appreciable for the irradiated sample indicative of overall more oxidized *N* species.

3.8. Dye Removal Tests

The dye sorption capability of all composites was tested towards methyl orange (MO) removal in water medium: MO was chosen as model pollutant for anionic azo-dyes due to its bio-accumulation risk and eco-toxicity [57]. Most of the samples exhibit very good performance in terms of dye removal (>95% for tests with 50 ppm MO starting concentration, Table S5). A closer look at the data shows a main role of the composite specific surface area, as the best performing samples have areas larger than 30 $m^2 g^{-1}$, in good agreement with the literature [14,20]. The 1 × 3 sample gave rise to the worst performance (barely 48% of dye removed), which could be related to its very low surface area and compact morphology. It should be noted that even this sample outperforms PANI_ref (MO removal 10%)[20].

However, surface area is not the only factor at play. For instance, by comparing the 3 × 3 and 1 × 2 composites, the sample with the larger surface area (24 vs. 21 $m^2 g^{-1}$, respectively) exhibited lower performance in terms of MO removal (respectively 85% and 92%). This result could be related to the higher PANI content of the 1 × 2 composite as it is well known that polyaniline sorption mechanism is based on both an anion-exchange process (Cl^- vs. dye) and short-range interactions, such as hydrogen bonding and π-π stacking [20,58,59]: thus, composites with a more accessible polymer structure and more sorption sites are characterized by better dye-sorption performances.

Samples retain good dye removal performance in a broad concentration range (10-200 ppm), displaying a linear increase in the dye sorbed amount (Figure S7). A stress test on a representative composite (1 × 1) was performed by reusing the material several times for the remediation of concentrated dye solutions (50 ppm) without any regeneration in between consecutive runs. The first two sorption tests show an almost complete dye removal, while afterwards the dye removal capacity starts to decrease as expected (Figure 8). Consecutive runs were carried out until an almost complete loss of the sorption properties was observed. A maximum sorption capacity of 62 $mg g^{-1}$ was determined, which favorably compares with literature results concerning the adsorption of acid red dyes by PANI-based materials [60,61] and activated carbon [62]. It should be noted that even after the maximum sorption capacity was reached, the initial sorption properties of the composite could be fully restored by simply immersing it in alkaline water for 24 h (20 mL of NaOH solution at pH around 10). Moreover, this regeneration approach enables to recover unaltered the sorbed dye, opening the door to its reusage in a circular economy perspective.

For the sake of comparability with real-life conditions, sorption tests were carried out also in simulated drinking water (Table S1). The sorption test exhibits comparable results with respect to the dye solution in the absence of electrolytes (94% vs. 96%, respectively). Moreover, in simulated drinking water, the sorption properties could be retained for many more consecutive runs leading to a notable increase in the total MO sorbed amount: after eleven reuses without regeneration, a 94 $mg g^{-1}$ dye-sorption capacity was measured. It should be noted that the stress test in simulated drinking water was stopped well before the sample sorption limit could be reached (Figure 8). In simulated drinking water, besides the dye molecules, there are several and more concentrated ions in solution, including chlorides. Such ions could lead to competitive adsorption at the polyaniline charged sites and the higher ionic strength could, on one hand, partially shield the dye molecules reducing their ability to interact with the PANI chains, while on the other hand, it could promote sites dissociation. In the pristine PANI composite, positively charged sorption sites are fully compensated by Cl^- counterions, which are mainly exchanged with the anionic dye during the first sorption test. In the subsequent cycles, dye molecules and chloride ions in solution compete for displacing adsorbed species (either dye molecules or chlorides) on the grounds of electrostatic interactions. All these competitive interactions cause a decrease in the percentage of removed MO, while postponing the sorbent saturation.
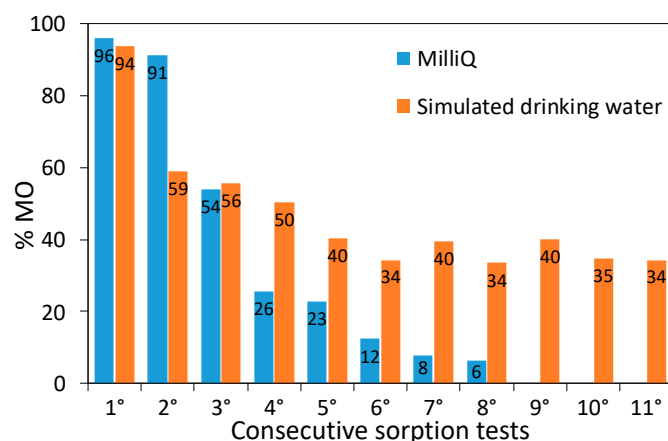
Figure 8. MO removal during sorption tests: consecutive runs of the 1 × 1 sample performed in both Milli-*Q* water and simulated drinking water.

3.9. Chromium Remediation Tests

Prompted by its optimal dye-removal performances, the 1 × 1 composite was also tested for the remediation of Cr(VI) in solution. Hexavalent chromium is a well-known toxic, carcinogenic and mutagenic species; on the other hand, its trivalent form, Cr(III), is about 1000 times less hazardous and can be removed by adsorption or precipitation (Cr(OH$_3$)) at neutral pH [63]: thus, most of the Cr(VI) abatement methods are based on its reduction to Cr(III) followed by the removal of the latter. However, the chemical reduction process consumes large quantities of reductants and generates high amounts of secondary waste. Polyaniline has been reported to reduce Cr(VI) to Cr(III) and to remove both the species by sorption [63]: both the sorption and reduction mechanisms are strongly pH dependent. The best sorption performances are achieved at pH 5, while the reduction is reported to be favored by strong acidic conditions (pH < 2) [63].

In the present work, tests were carried out at pH 1.8 using two different Cr(VI) concentrations (10 and 50 ppm), well within the range of chromium concentration in industrial wastewaters [64]. In both cases, the 1 × 1 composite was able to reduce > 99% of the Cr(VI) and to directly remove 50% of the total chromium in solution in just 20 minutes. Furthermore, the present composite outperforms PANI_ref in terms of both Cr(VI) reduction and total chromium removal results; as a matter of fact, the latter reduces only 30% of Cr(VI) and removes merely 2% of the total chromium in a 10 ppm solution.

Stress tests were carried out also in this case: after retrieval by centrifugation, the 1 × 1 composite was reused for five consecutive removal tests without any intermediate regeneration treatment. In order to simulate experimental conditions close to real life applications, stress tests were carried out without adjusting the pH value. Five consecutive cycles were carried out using either 10 ppm and 50 ppm Cr(VI) solutions at spontaneous pH (Figure 9). The 1 × 1 composite was able to maintain over 90% Cr(VI) reduction even at the fifth reuse at the highest adopted chromium concentration, reaching a total Cr(VI) reduction capacity of 98 mg/g. This performance favorably compares with previous literature reports [63,65–67]; in this respect, it should be noted that the cycle test was stopped well before the sample sorption limit could be reached.

Total chromium removal markedly increases during the cycles: from values close to 50% during the first test to over 96% at the fifth reuse. This behavior can be related to the progressive spontaneous increase of pH in the suspension (from pH 1.8 for the first tests to values around 5 in the last tests). As a matter of fact, the sorption mechanism of cations is favored with pH values around 5, while it is hindered at pH ≤ 2 due to the charge repulsion between the positively charged polyaniline and Cr(III) cations. Concerning anions removal, such as Cr(VI) mainly present in solution as HCrO$_4^-$, two adsorption mechanisms can be proposed. The first one is based on a dopant change, whereas the second mechanism involves electrostatic interactions among the anion and the positive iminic groups of the polymer. It should be noted that the present composite displays unaltered Cr(VI) reduction capacity in a broad range of pH values, which enables to modulate the

sorption performance at will. When a complete abatement of all chromium species is required, pH values around 5 can be adopted. On the contrary, if Cr(III) species are to be separately recovered (as required in a circular economy perspective), strong acidic conditions are the optimal choice.
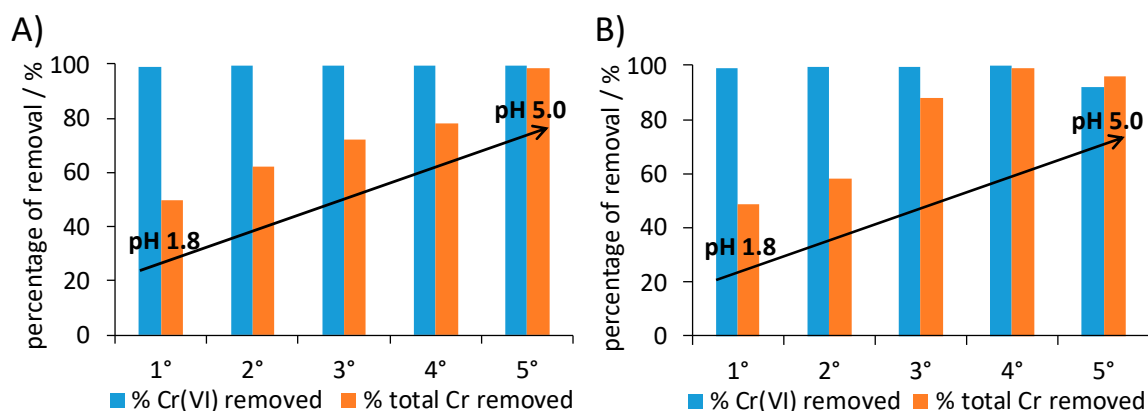

Figure 9. Consecutive chromium removal tests for 1 × 1 nanocomposite: **A**) 10 ppm and **B**) 50 ppm initial Cr(VI) concentration. For each test, the removal of Cr(VI) (± 0.04%) and of total chromium (± 4%) are reported.

These results demonstrate that the synthesized composite materials are characterized by a fast and efficient Cr(VI) removal capacity, adjustable chromium sorption properties, as well as a high degree of reusability, even in the total absence of regeneration treatments. Moreover, preliminary tests have shown that a quick washing with a 0.05 M HCl solution can be adopted to reactivate the composites.

4. Discussion

The main characteristic of the synthetic pathway herein proposed is the clear distinction between the oligomerization and polymerization steps. This two-step reaction mechanism points towards different roles played by TiO_2/UV with respect to H_2O_2, which are both essential for the PANI formation. The first step involves the adsorption of aniline dimers at the oxide surface, as shown by both FTIR and XPS spectra exhibiting a loss of surface hydroxylation and a notable second component in the Ti 2p spectra. The latter effect is more marked in the presence of UV irradiation, in accordance with the literature reporting an increased omniphilicity of light-irradiated TiO_2 [68]. This initial step is crucial to promote the final PANI crystallinity and porous morphology, which can be related to the controlled and oriented growth of the oligomer chains at the oxide surface, explaining the unique crystallinity degree of our samples with respect to literature composites [28,36,37,39,40].

Light irradiation is fundamental to promote the dimer-TiO_2 interaction as well as the formation of radicals via photocatalytic reactions, which can act as initiators of the oligomerization step. In this respect, XPS and MS spectra consistently show the occurrence of radical-assisted oxidative processes in the UV irradiated sample, as also supported by literature studies about the photocatalytic degradation of aniline by TiO_2 [69–71].

It should be underlined that the reaction cannot proceed further without the addition of H_2O_2, as clearly shown by the change in color from violet to dark green, characteristic of polyaniline, upon H_2O_2 addition. Oxygen peroxide is known to act as both a radical source initiating PANI synthesis, as well as an oxidant supporting the polymer growth [72]. In PANI_ref synthesis, previous studies have shown that H_2O_2 dissociation in the presence of a catalyst can produce radical species (HO·) able to promote the formation of initiators (aniline dimer radicals) [72]. These are crucial for the first part of the reaction, which follows a radical mechanism. Afterwards, H_2O_2 acts as an oxidant during the growth of polymer chains [73]. However, it is still unclear whether the more oxidized form of polyaniline (pernigraniline) is initially produced and then spontaneously decays to the more stable form of emeraldine, or whether the more reduced form of PANI (leucoemeraldine) is immediately

synthesized and then gradually oxidized to emeraldine [74]. In the present study, characterizations confirmed that the formation of active species (aniline dimer radicals) takes place on the TiO_2 surface in the first part of the reaction, thus guaranteeing the formation of PANI oligomers. Hence, in our hypothesis, hydrogen peroxide plays mainly the role of the oxidant during polymer growth.

The H_2O_2 amount plays a major role on the final materials properties, promoting on one side an increase in the PANI content, which comes at the cost of a lower crystallinity, altered benzenoid/quinoid ratio, and worsened morphological properties. In this respect, the PANI_ref synthesis involves a homogeneous catalysis and a much higher H_2O_2 : aniline dimer ratio, leading to poor structural and morphological features. Here 5-times lower H_2O_2 : aniline dimer ratios can be successfully employed for the synthesis due to the synergistic role played by H_2O_2 and TiO_2/UV. It is hard to assert whether H_2O_2 promotes only the growth of adsorbed chains on the oxide surface or elicits reactions in homogeneous phase, as *e.g.* in PANI_ref. However, on the grounds of TGA and MS findings, we can suggest that, at low H_2O_2 amounts, the growth is driven by the adsorbed oligomers. At increasing H_2O_2 quantities, evidence of a parallel homogeneous pathway becomes instead appreciable. For instance, TGA curves of 1 × 2 and 1 × 3 samples are consistent with weaker polyaniline-TiO_2 interactions and MS spectra present soluble components in common with the PANI_ref spectrum, at variance with those shown by the 1 × 1 sample.

The insight gained into the relative roles of TiO_2/UV and H_2O_2 on the reaction mechanism allows us to modulate the composite properties in a broad range. The nanocomposite composition, crystallinity, morphology and conjugation degree can all be modified by working on the reagent ratios to suit the desired application. In the present case, the composite performance could be enhanced mainly by increasing the specific surface area using low H_2O_2 : aniline dimer ratios. In this respect, the TiO_2 content in the nanocomposite could be increased without affecting the materials characteristics, a much desired feature for applications directly exploiting the TiO_2 semiconductor properties. On the other hand, increasing H_2O_2 amount during synthesis leads to poorer structural and morphological properties. However, even at the highest H_2O_2 : aniline dimer ratios tested in the present work, the resulting composites displayed promoted crystallinity and surface areas with respect to purely homogeneous synthetic pathways (PANI_ref and literature composites), enabling us to tune the PANI content in the nanocomposite to a wider extent (up to 75%w).

5. Conclusions

PANI-TiO_2 nanocomposites prepared via UV-light mediated green procedure were here studied and applied to pollutant removal in water. The preparation of PANI-TiO_2 composites has been quite extensively reported in the literature by using both preformed particles and TiO_2 sols/gels [12,29,37,38,75,76]. However, the present synthesis differs from the state-of-the-art as the photocatalytic activity of TiO_2 is directly exploited to initiate a green polymerization process, leading to materials with unique properties. Here, we varied the H_2O_2 and TiO_2 amounts to demonstrate their different but essential roles on the composite thermal, optical, structural and morphological properties. The first reaction step, driven by TiO_2 and UV irradiation, was found to be a radical process which promotes the final composite crystallinity and polymer-oxide interaction. The H_2O_2 addition is needed for PANI preparation and its amount has a crucial role on the reaction pathway. Low H_2O_2 quantities can preferentially promote the growth of oligomer chains adsorbed on TiO_2 particles, giving rise to highly porous, large surface area nanocomposites with good crystallinity but lower PANI-content. On the other hand, high H_2O_2 amounts seem to promote a homogenous polymer formation process, which leads to nanocomposites with higher PANI content and thermal stability, at the expense of their crystallinity and porous morphology. However, even at the highest tested H_2O_2 amount, the present nanocomposites display characteristic structural and morphological features that differentiate them from PANI samples from homogenous catalysis reaction (PANI_ref) as well as from composites prepared by conventional oxidative polymerization routes. These results enabled us to tune the composite properties in order to adapt them to different applications. In the present case, materials prepared with low H_2O_2 amounts showed the best performance in terms of pollutant removal capability, exhibiting a fast and complete MO and Cr(VI) abatement in tests on a

broad concentration range. In the literature PANI-TiO₂ composites are mostly applied as photocatalyst for pollutant degradation [29,38,75,76], with the inherent limitations of this approach such as slow reaction kinetics, interfering effect of common electrolytes and possible accumulation of stable and toxic by-products. In this respect, the prepared nanocomposites show instead excellent sorption properties that can be used even in the presence of concentrated electrolytes (e.g., chlorides, bicarbonates), enabling the recovery of the pristine molecule upon mild treatments. Moreover, in the case of Cr(VI) abatement, the metal ion reduction is here obtained without the need of additional reagents (as opposed to the case of photocatalysis in which a hole scavenger is needed) and with the concurrent sorption of Cr(III). Furthermore, the composite showed excellent reusability, even in the total absence of regeneration treatments and under real-life conditions, as shown by the good performance in simulated drinking water. Future work will investigate the immobilization of the nanocomposite on macroscopic devices in order to simplify the recovery at the end of the treatment.

Supplementary Materials: The following are available online at https://www.mdpi.com/2079-4991/10/3/441/s1, Table S1: simulated drinking water composition, Figure S1: TGA and DTG curves of 1 × 1 composite compared to PANI-ref, Figure S2: FTIR spectra of all composites, Figure S3: FTIR spectra of PANI_ref, 3 × 1 composite and TiO₂, Figure S4: UV-vis curves in DMF of all samples, Table S2: dependence of the H1/H2 ratio from the H₂O₂/aniline dimer molar ratio, Table S3: attributions to MS signals, Figure S5: FTIR spectra of samples from oligomerization step study, Table S4: elemental composition from XPS survey, Figure S6: high resolution XPS spectra in the O 1s and N 1s regions of samples from oligomerization step study, Table S5: percentage of MO removed during sorption tests for all samples, Figure S7: MO removal capability as a function of the MO initial concentration.

Author Contributions: Conceptualization, C.C., C.D.P., D.M., E.F., S.A.; methodology, E.F. and D.M.; investigation, C.C..; resources, S.A. and C.D.P.; data curation, C.C.; writing—original draft preparation, D.M. and E.F.; writing—review and editing, S.A. and C.D.P.; supervision, S.A. All authors have read and agreed to the published version of the manuscript.

Conflicts of Interest: The authors declare no conflict of interest.

References

1. Kumar, R.; Ansari, M.O.; Parveen, N.; Oves, M.; Barakat, M.A.; Alshahri, A.; Khan, M.Y.; Cho, M.H. Facile route to a conducting ternary polyaniline@TiO₂/GN nanocomposite for environmentally benign applications: photocatalytic degradation of pollutants and biological activity. *RSC Adv.* **2016**, *6*, 111308–111317.
2. Zhang, J.; Zhao, Z.; Xia, Z.; Dai, L. A metal-free bifunctional electrocatalyst for oxygen reduction and oxygen evolution reactions. *Nat. Nanotechnol.* **2015**, *10*, 444–452.
3. Wang, P.H.; Wang, T.L.; Lin, W.C.; Lin, H.Y.; Lee, M.H.; Yang, C.H. Enhanced supercapacitor performance using electropolymerization of self-doped polyaniline on carbon film. *Nanomaterials* **2018**, *8*.
4. Wang, L.; Feng, X.; Ren, L.; Piao, Q.; Zhong, J.; Wang, Y.; Li, H.; Chen, Y.; Wang, B. Flexible Solid-State Supercapacitor Based on a Metal–Organic Framework Interwoven by Electrochemically-Deposited PANI. *J. Am. Chem. Soc.* **2015**, *137*, 4920–4923.
5. Eftekhari, A.; Li, L.; Yang, Y. Polyaniline supercapacitors. *J. Power Sources* **2017**, *347*, 86–107.
6. Shehzad, M.A.; Liang, X.; Yasmin, A.; Ge, X.; Xiao, X.; Zhu, Y.; Ge, Z.; Wang, Y.; Wu, L.; Xu, T. Angioplasty mimetic stented ion transport channels construct durable high-performance membranes. *J. Mater. Chem. A* **2019**, *7*, 10030–10040.
7. Cao, G.; Gao, X.; Wang, L.; Cui, H.; Lu, J.; Meng, Y.; Xue, W.; Cheng, C.; Tian, Y.; Tian, Y. Easily synthesized polyaniline@cellulose nanowhiskers better tune network structures in Ag-based adhesives: Examining the improvements in conductivity, stability, and flexibility. *Nanomaterials* **2019**, *9*.

8. Ge, X.; He, Y.; Plachy, T.; Kazantseva, N.; Saha, P.; Cheng, Q. Hierarchical PANI/NiCo-LDH core-shell composite networks on carbon cloth for high performance asymmetric supercapacitor. *Nanomaterials* **2019**, *9*.

9. Jiao, S.; Li, T.; Xiong, C.; Tang, C.; Li, H.; Zhao, T.; Dang, A. A facile method to prepare silver doped graphene combined with polyaniline for high performances of filter paper based flexible electrode. *Nanomaterials* **2019**, *9*.

10. Luo, C.; Wang, Y.; Li, X.; Jiang, X.; Gao, P.; Sun, K.; Zhou, J.; Zhang, Z.; Jiang, Q. An optical sensor with polyaniline-gold hybrid nanostructures for monitoring pH in saliva. *Nanomaterials* **2017**, *7*, 1–11.

11. Michalska, A.; Golczak, S.; Langer, K.; Langer, J.J. Micro-and nanostructured polyaniline for instant identification of metal ions in solution. *Nanomaterials* **2019**, *9*.

12. Wang, N.; Li, J.; Lv, W.; Feng, J.; Yan, W. RSC Advances excellent adsorption performance on acid red G. *RSC Adv.* **2015**, *5*, 21132–21141.

13. He, J.; To, J.W.F.; Psarras, P.C.; Yan, H.; Atkinson, T.; Holmes, R.T.; Nordlund, D.; Bao, Z.; Wilcox, J. Tunable Polyaniline-Based Porous Carbon with Ultrahigh Surface Area for CO_2 Capture at Elevated Pressure. *Adv. Energy Mater.* **2016**, *6*, 1502491.

14. Della Pina, C.; De Gregorio, M.A.; Clerici, L.; Dellavedova, P.; Falletta, E. Polyaniline (PANI): an innovative support for sampling and removal of VOCs in air matrices. *J. Hazard. Mater.* **2018**, *344*, 308–315.

15. Zhang, J.; Han, J.; Wang, M.; Guo, R. Fe_3O_4/PANI/MnO_2 core-shell hybrids as advanced adsorbents for heavy metal ions. *J. Mater. Chem. A* **2017**, *5*, 4058–4066.

16. Gong, K.; Guo, S.; Zhao, Y.; Hu, Q.; Liu, H.; Sun, D.; Li, M.; Qiu, B.; Guo, Z. Bacteria cell templated porous polyaniline facilitated detoxification and recovery of hexavalent chromium. *J. Mater. Chem. A* **2018**, *6*, 16824–16832.

17. Shumakovich, G.; Kurova, V.; Vasil'eva, I.; Pankratov, D.; Otrokhov, G.; Morozova, O.; Yaropolov, A. Laccase-mediated synthesis of conducting polyaniline. *J. Mol. Catal. B Enzym.* **2012**, *77*, 105–110.

18. Wu, Y.; Wang, J.; Ou, B.; Zhao, S.; Wang, Z.; Wang, S. Electrochemical preparation of polyaniline nanowires with the used electrolyte solution treated with the extraction process and their electrochemical performance. *Nanomaterials* **2018**, *8*, 1–13.

19. Bhadra, S.; Singha, N.K.; Khastgir, D. Electrochemical synthesis of polyaniline and its comparison with chemically synthesized polyaniline. *J. Appl. Polym. Sci.* **2007**, *104*, 1900–1904.

20. Cionti, C.; Della Pina, C.; Meroni, D.; Falletta, E.; Ardizzone, S. Triply green polyaniline: UV irradiation-induced synthesis of a highly porous PANI/TiO_2 composite and its application in dye removal. *Chem. Commun.* **2018**, *54*, 10702–10705.

21. Rimoldi, L.; Meroni, D.; Falletta, E.; Pifferi, V.; Falciola, L.; Cappelletti, G.; Ardizzone, S. Emerging pollutant mixture mineralization by TiO_2 photocatalysts. The role of the water medium. *Photochem. Photobiol. Sci.* **2017**, *16*, 60–66.

22. Ansari, R.; Keivani, M.B. Polyaniline Conducting Electroactive Polymers Thermal and Environmental Stability Studies. *E-Journal Chem.* **2006**, *3*, 202–217.

23. Li, X.; Wang, G.; Li, X.; Lu, D. Surface properties of polyaniline/nano-TiO_2 composites. *Appl. Surf. Sci.* **2004**, *229*, 395–401.

24. Lee, I.S.; Lee, J.Y.; Sung, J.H.; Choi, H.J. Synthesis and electrorheological characteristics of polyaniline-titanium dioxide hybrid suspension. *Synth. Met.* **2005**, *152*, 173–176.

25. Gurunathan, K.; Trivedi, D.C. Studies on polyaniline and colloidal TiO_2 composites. *Mater. Lett.* **2000**, *45*, 262–268.

26. Wang, S.; Tan, Z.; Li, Y.; Sun, L.; Zhang, T. Synthesis, characterization and thermal analysis of polyaniline/ZrO_2 composites. *Thermochim. Acta* **2006**, *441*, 191–194.

27. Ansari, M.O.; Mohammad, F. Sensors and Actuators B : Chemical Thermal stability , electrical conductivity and ammonia sensing studies on p -toluenesulfonic acid doped polyaniline : titanium dioxide (p TSA/Pani:TiO_2) nanocomposites. *Sensors Actuators B. Chem.* **2011**, *157*, 122–129.

28. Schnitzler, D.C.; Meruvia, M.S.; Hümmelgen, I.A.; Zarbin, A.J.G. Preparation and Characterization of Novel Hybrid Materials Formed from (Ti,Sn)O_2 Nanoparticles and Polyaniline. *Chem. Mater.* **2003**, *15*, 4658–4665.

29. Gilja, V.; Novaković, K.; Travas-Sejdic, J.; Hrnjak-Murgić, Z.; Roković, M.K.; Žic, M. Stability and synergistic effect of polyaniline/TiO_2 photocatalysts in degradation of Azo dye in wastewater. *Nanomaterials* **2017**, *7*.

30. Alves, W.F.; Venancio, E.C.; Leite, F.L.; Kanda, D.H.F.; Malmonge, L.F.; Malmonge, J.A.; Mattoso, L.H.C. Thermo-analyses of polyaniline and its derivatives. *Thermochim. Acta* **2010**, *502*, 43–46.
31. Chandrakanthi, N.; Careem, M.A. Thermal stability of polyaniline. *Polym. Bull.* **2000**, *44*, 101–108.
32. Lu, X.; Tan, C.Y.; Xu, J.; He, C. Thermal degradation of electrical conductivity of polyacrylic acid doped polyaniline: Effect of molecular weight of the dopants. *Synth. Met.* **2003**, *138*, 429–440.
33. Nabid, M.R.; Golbabaee, M.; Moghaddam, A.B. Polyaniline/TiO₂ Nanocomposite : Enzymatic Synthesis and Electrochemical Properties. *Int. J. Electrochem. Sci.* **2008**, *3*, 1117–1126.
34. Li, X.; Chen, W.; Bian, C.; He, J.; Xu, N.; Xue, G. Surface modification of TiO₂ nanoparticles by polyaniline. *Appl. Surf. Sci.* **2003**, *217*, 16–22.
35. Pouget, J.P.; Józefowicz, M.E.; Epstein, A.J.; Tang, X.; MacDiarmid, A.G. X-ray Structure of Polyaniline. *Macromolecules* **1991**, *24*, 779–789.
36. Katoch, A.; Burkhart, M.; Hwang, T.; Kim, S.S. Synthesis of polyaniline/TiO₂ hybrid nanoplates via a sol–gel chemical method. *Chem. Eng. J.* **2012**, *192*, 262–268.
37. Singh, R.; Choudhary, R.B.; Kandulna, R. Robust optical and electrical properties of TiO₂-sensitized polymeric (PANI–TiO₂) nanocomposites for hybrid solar cell application. *Bull. Mater. Sci.* **2019**, *42*, 202.
38. Reddy, K.R.; Karthik, K.V.; Prasad, S.B.B.; Soni, S.K.; Jeong, H.M.; Raghu, A. V Enhanced photocatalytic activity of nanostructured titanium dioxide/polyaniline hybrid photocatalysts. *Polyhedron* **2016**, *120*, 169–174.
39. Zhang, L.; Wan, M. Polyaniline/TiO₂ Composite Nanotubes. *J. Phys. Chem. B* **2003**, *107*, 6748–6753.
40. Lu, J.; Zhang, X.; Gao, H.; Cui, W. Three-dimensional structure of PANI/CdS NRs-SiO₂ hydrogel for photocatalytic hydrogen evolution with high activity and stability. *Nanomaterials* **2019**, *9*.
41. Rimoldi, L.; Pargoletti, E.; Meroni, D.; Falletta, E.; Cerrato, G.; Turco, F.; Cappelletti, G. Concurrent role of metal (Sn, Zn) and N species in enhancing the photocatalytic activity of TiO₂ under solar light. *Catal. Today* **2018**, *313*, 40–46.
42. Giannakoudakis, D.A.; Bandosz, T.J. Defectous UiO-66 MOF Nanocomposites as Reactive Media of Superior Protection against Toxic Vapors. *ACS Appl. Mater. Interfaces* **2019**, acsami.9b17314.
43. Falletta, E.; Costa, P.; Della Pina, C.; Lanceros-Mendez, S. Development of high sensitive polyaniline based piezoresistive films by conventional and green chemistry approaches. *Sensors Actuators, A Phys.* **2014**, *220*, 13–21.
44. Šeděnková, I.; Trchová, M.; Stejskal, J. Thermal degradation of polyaniline films prepared in solutions of strong and weak acids and in water - FTIR and Raman spectroscopic studies. *Polym. Degrad. Stab.* **2008**, *93*, 2147–2157.
45. Meroni, D.; Lo Presti, L.; Di Liberto, G.; Ceotto, M.; Acres, R.G.; Prince, K.C.; Bellani, R.; Soliveri, G.; Ardizzone, S. A Close Look at the Structure of the TiO₂-APTES Interface in Hybrid Nanomaterials and Its Degradation Pathway: An Experimental and Theoretical Study. *J. Phys. Chem. C* **2017**, *121*, 430–440.
46. Della Pina, C.; Ferretti, A.M.; Ponti, A.; Falletta, E. A green approach to magnetically-hard electrically-conducting polyaniline/CoFe₂O₄ nanocomposites. *Compos. Sci. Technol.* **2015**, *110*, 138–144.
47. Albuquerque, J.E.; Mattoso, L.H.C.; Balogh, D.T.; Faria, R.M.; Masters, J.G.; MacDiarmid, A.G. Simple method to estimate the oxidation state of polyanilines. *Synth. Met.* **2000**, *113*, 19–22.
48. Laska, J.; Widlarz, J. Spectroscopic and structural characterization of low molecular weight fractions of polyaniline. *Polymer (Guildf).* **2005**, *46*, 1485–1495.
49. Dolan, A.R.; Wood, T.D. Synthesis and characterization of low molecular weight oligomers of soluble polyaniline by electrospray ionization mass spectrometry. *Synth. Met.* **2004**, *143*, 243–250.
50. Rimoldi, L.; Giordana, A.; Cerrato, G.; Falletta, E.; Meroni, D. Insights on the photocatalytic degradation processes supported by TiO₂/WO₃ systems. The case of ethanol and tetracycline. *Catal. Today* **2019**, *328*, 210–215.
51. Parveen, N.; Ansari, M.O.; Cho, M.H. Route to High Surface Area, Mesoporosity of Polyaniline-Titanium Dioxide Nanocomposites via One Pot Synthesis for Energy Storage Applications. *Ind. Eng. Chem. Res.* **2016**, *55*, 116–124.
52. Li, S.C.; Diebold, U. Reactivity of TiO₂ rutile and anatase surfaces toward nitroaromatics. *J. Am. Chem. Soc.* **2010**, *132*, 64–66.
53. Li, S.C.; Losovyj, Y.; Paliwal, V.K.; Diebold, U. Photoemission study of azobenzene and aniline adsorbed on TiO₂ anatase (101) and rutile (110) surfaces. *J. Phys. Chem. C* **2011**, *115*, 10173–10179.

54. Saroyan, H.S.; Bele, S.; Giannakoudakis, D.A.; Samanidou, V.F.; Bandosz, T.J.; Deliyanni, E.A. Degradation of endocrine disruptor, bisphenol-A, on an mixed oxidation state manganese oxide/modified graphite oxide composite: A role of carbonaceous phase. *J. Colloid Interface Sci.* **2019**, *539*, 516–524.

55. Golczak, S.; Kanciurzewska, A.; Fahlman, M.; Langer, K.; Langer, J.J. Comparative XPS surface study of polyaniline thin films. *Solid State Ionics* **2008**, *179*, 2234–2239.

56. Li, C.; Wang, Z.; Li, S.; Cheng, J.; Zhang, Y.; Zhou, J.; Yang, D.; Tong, D.; Wang, B. Interfacial Engineered Polyaniline/Sulfur-Doped TiO_2 Nanotube Arrays for Ultralong Cycle Lifetime Fiber-Shaped , Solid-State Supercapacitors. *ACS Appl. Mater. Interfaces* **2018**, *10*, 18390–18399.

57. Reif, A.; Freemann, H.S. *Environmental Chemistry of Dyes and Pigments*; Wiley, Ed.; New York, 1996.

58. Kumar, R.; Ansari, M.O.; Parveen, N.; Barakat, M.A.; Cho, M.H. Simple route for the generation of differently functionalized PVC@graphene-polyaniline fiber bundles for the removal of Congo red from wastewater. *RSC Adv.* **2015**, *5*, 61486–61494.

59. Yan, B.; Chen, Z.; Cai, L.; Chen, Z.; Fu, J.; Xu, Q. Fabrication of polyaniline hydrogel: Synthesis, characterization and adsorption of methylene blue. *Appl. Surf. Sci.* **2015**, *356*, 39–47.

60. Mahanta, D.; Madras, G.; Radhakrishnan, S.; Patil, S. Adsorption of Sulfonated Dyes by Polyaniline Emeraldine Salt and Its Kinetics. *J. Phys. Chem. B* **2008**, *112*, 10153–10157.

61. Ahmad, R.; Kumar, R. Conducting Polyaniline/Iron Oxide Composite: A Novel Adsorbent for the Removal of Amido Black 10B. *J. Chem. Eng. Data* **2010**, *55*, 3489–3493.

62. Gómez, V.; Larrechi, M.S.; Callao, M.P. Kinetic and adsorption study of acid dye removal using activated carbon. *Chemosphere* **2007**, *69*, 1151–1158.

63. Guo, X.; Fei, G.T.; Su, H.; De Zhang, L. High-performance and reproducible polyaniline nanowire/tubes for removal of Cr(VI) in aqueous solution. *J. Phys. Chem. C* **2011**, *115*, 1608–1613.

64. Sarin, V.; Pant, K.K. Removal of chromium from industrial waste by using eucalyptus bark. *Bioresour. Technol.* **2006**, *97*, 15–20.

65. Zhang, R.; Ma, H.; Wang, B. Removal of Chromium (VI) from Aqueous Solutions Using Polyaniline Doped with Sulfuric Acid. **2010**, 9998–10004.

66. Kumar, R.; Ansari, M.O.; Barakat, M.A. DBSA doped polyaniline/multi-walled carbon nanotubes composite for high efficiency removal of Cr(VI) from aqueous solution. *Chem. Eng. J.* **2013**, *228*, 748–755.

67. Karthik, R.; Meenakshi, S. Removal of hexavalent chromium ions using polyaniline/silica gel composite. *J. Water Process Eng.* **2014**, *1*, 37–45.

68. Zuo, J.; Torres, E. Comparison of Adsorption of Mercaptopropyltrimethoxysilane on Amphiphilic TiO_2 and Hydroxylated SiO_2. *Langmuir* **2010**, *26*, 15161–15168.

69. Kumar, A.; Mathur, N. Photocatalytic degradation of aniline at the interface of TiO_2 suspensions containing carbonate ions. *J. Colloid Interface Sci.* **2006**, *300*, 244–252.

70. Canle L., M.; Santaballa, J.A.; Vulliet, E. On the mechanism of TiO_2-photocatalyzed degradation of aniline derivatives. *J. Photochem. Photobiol. A Chem.* **2005**, *175*, 192–200.

71. Wenhua, L.; Hong, L.; Sao, C.; Jianqing, Z.; Chunan, C. Kinetics of photocatalytic degradation of aniline in water over TiO_2 supported on porous nickel. *J. Photochem. Photobiol. A Chem.* **2000**, *131*, 125–132.

72. Castagna, R.; Tunesi, M.; Saglio, B.; Della Pina, C.; Sironi, A.; Albani, D.; Bertarelli, C.; Falletta, E. Ultrathin electrospun PANI nanofibers for neuronal tissue engineering. *J. Appl. Polym. Sci.* **2016**, *133*, 43885.

73. Sapurina, I.; Stejskal, J. The mechanism of the oxidative polymerization of aniline and the formation of supramolecular polyaniline structures. *Polym. Int.* **2008**, *57*, 1295–1325.

74. Ćirić-Marjanović, G. Recent advances in polyaniline research: Polymerization mechanisms, structural aspects, properties and applications. *Synth. Met.* **2013**, *177*, 1–47.

75. Xu, J.; Wang, X.; Yuan, X.; Tao, J.; Peng, S.; Yang, W.; Dong, X.; Zhang, C.; Luo, Y. Polyaniline modified mesoporous titanium dioxide that enhances oxo-biodegradation of polyethylene films for agricultural plastic mulch application. *Polym. Int.* **2019**, *68*, 1332–1340.

76. Vaez, M.; Alijani, S.; Omidkhah, M.; Zarringhalam Moghaddam, A. Synthesis, characterization and optimization of N-TiO_2/PANI nanocomposite for photodegradation of acid dye under visible light. *Polym. Compos.* **2018**, *39*, 4605–4616.